

**Working notes:**  
Detailed statistical analysis of dark matter  
annihilation at the Galactic Centre with  
Fermi-LAT

Tesla Jeltema, Guðlaugur Jóhannesson, Grace Dupuis,  
Elinore Roebber, Antoine Recanati, Pat Scott,  
Charlotte Strece, Andrea Chiappo & Roberto Trotta  
(+some initial involvement from Johann Cohen-Tanugi,  
Jan Conrad, Joakim Edsjö, Eric Nuss,  
Troy Porter, Stefano Profumo & Roberto Ruiz de Austri)

Oct 2014

## 1 Goals

The goal of our analysis is to provide a statistically-convergent scan over the parameter space of generic annihilating WIMP models, testing their viability in light of Fermi observations of the Galactic Centre region and deriving robust constraints on the WIMP parameters. In particular, one of the main goals is to account properly for uncertainties in diffuse and point source modelling. Our model parameter space consists of the WIMP mass, annihilation cross-section and annihilation branching fractions into 10 different SM final states, an 11-parameter diffuse background model, 7 parameters per point source, and 4 parameters for the dark matter profile. Our final analysis aims to achieve statistically sound confidence regions from a profile likelihood analysis, for all parameters of interest. This will provide a far more general and statistically complete analysis than standard upper limit calculations based on assumed final states, and other analyses based on a small number of diffuse models.

In particular, the distinctive feature of this analysis is to include a raft of uncertainties as nuisance parameters in scans, allowing their effects to be profiled over. This translates into constraints on the WIMP properties that fully account for relevant astrophysical uncertainties. These uncertainties include background modelling, point source contributions, the dark matter density profile, the systematic error associated with the LAT effective area, and a full treatment of the LAT energy dispersion (absent from `gtlike`).

## 2 Methodology

The analysis proceeds via a series of nested sampling and differential evolution scans over the WIMP, point source and background parameter spaces, with the objective function given by the likelihood function. The likelihood is a binned Poissonian measure based on observed event counts in the direction of the Galactic Centre (identical to the binned likelihood implemented in the Segue 1 CMSSM analysis, and very similar to that implemented in ScienceTools). The exact ROI is freely configurable in the code, but we are mostly working with a  $10\times 10$  degree region centred on the GC. Instrumental effects are included via a full forward-folding with the LAT IRFs of every model in the parameter space, using the FLATLIB package developed for the Segue 1 CMSSM analysis. The systematic error in the LAT effective area is marginalised over at the likelihood level in a semi-Bayesian manner. Further uncertainties (background model, point sources, DM profile) are included as explicitly parameterised models with nuisance parameters that are simultaneously fit with the WIMP properties, and hence scanned over in the same manner as actual model parameters.

## 3 Progress to date

So far we have:

1. Developed DMBAYES, a modified version of the SUPERBAYES package, to perform the nested sampling+differential evolution scan over the WIMP parameter space. DMBAYES works with generic WIMP DM via an interface to DMFIT.
2. Coupled DMBAYES to FLATLIB
3. Written relevant likelihood and source modelling routines for the Galactic Centre
4. Implemented some rudimentary halo-marginalisation capabilities
5. Simulated a series of pure DM GC signals using `gtobssim`
6. Used these simulations to extensively test and tune DMBayes. An example DM-only reconstruction is given in Fig. 1.
7. Added the publicly-available diffuse background models (ring and isotropic) to DMBayes as tests
8. Simulated DM GC signals with backgrounds
9. Successfully reconstructed the DM model using DMBAYES in the presence of said backgrounds (Fig. 2).
10. Resolved a large number of technical and architecture-specific instabilities encountered when running early versions of DMBayes.

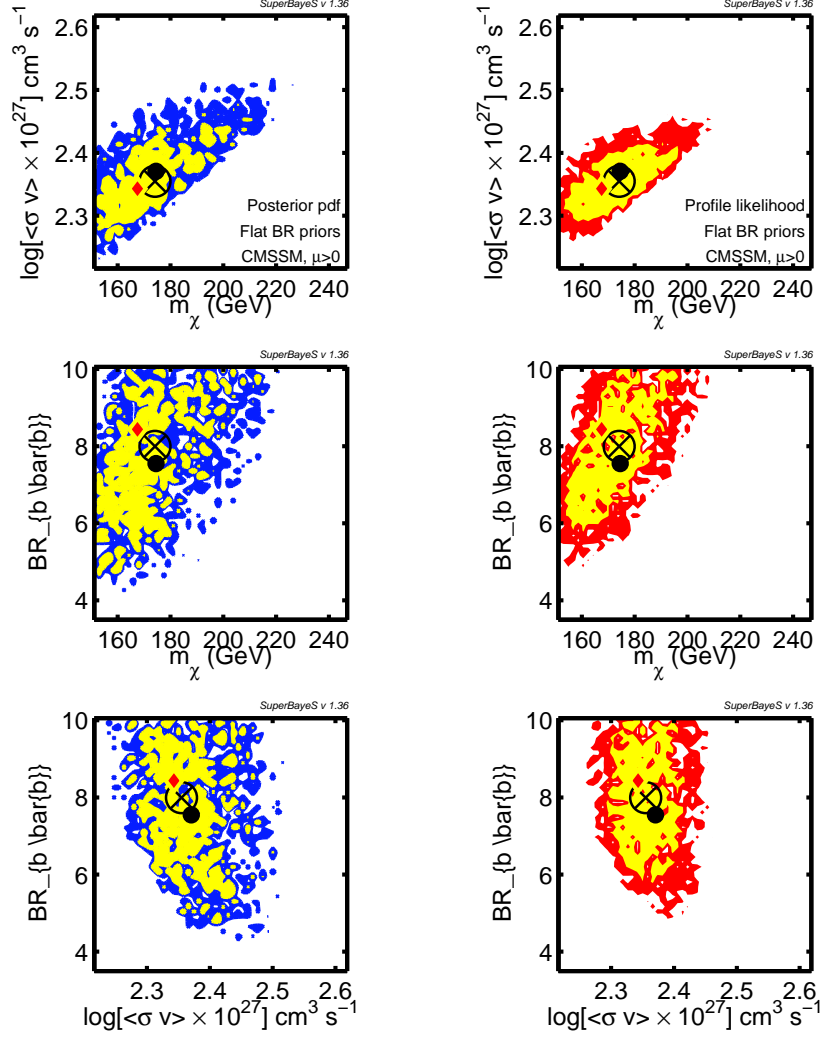


Figure 1: Reconstructed DM parameters using DMBAYES and FLATLIB, for a simulated pure DM signal at the Galactic Centre. The left (right) plot gives marginalised posterior PDFs (profile likelihoods), and shading indicates 1 and 2 $\sigma$  credible (confidence) intervals. Crosses indicate the best fit, bullets the posterior mean, and red/yellow diamonds the true parameter values. (Ignore annotations referring to CMSSM and SUPERBAYES)

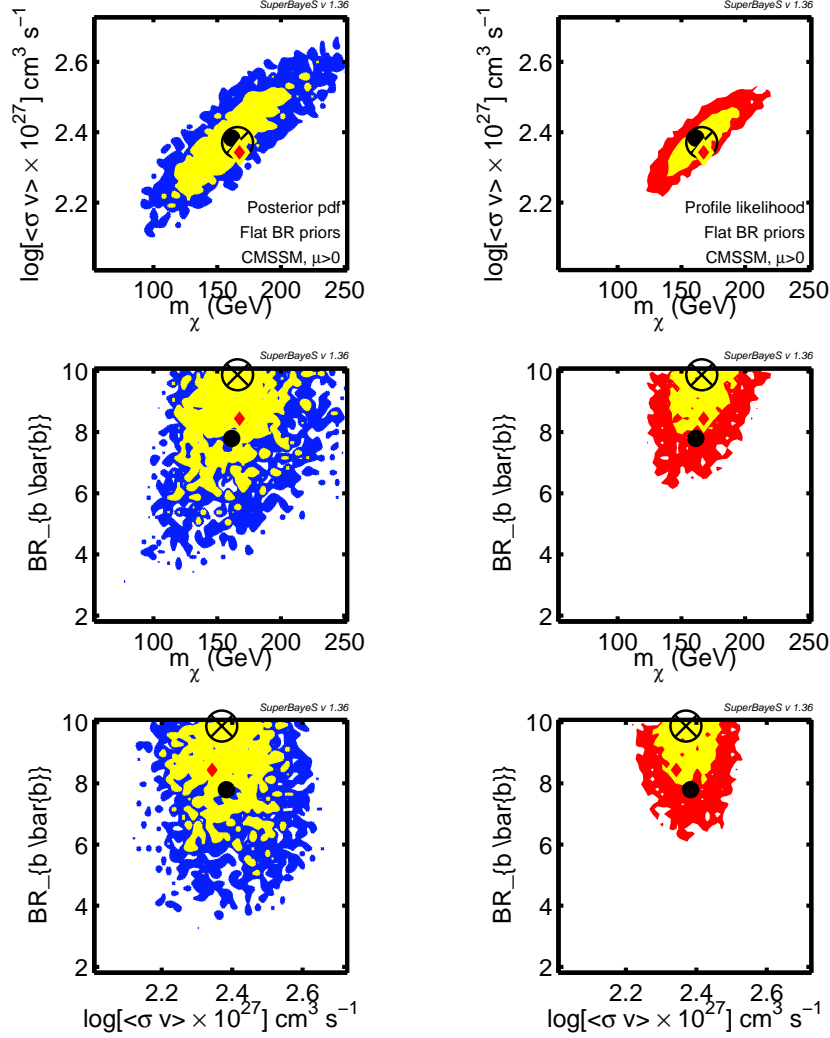


Figure 2: Reconstructed DM parameters using DMBAYES and FLATLIB in the presence of simulated background noise (based on public Galactic and isotropic background models). The left (right) plot gives marginalised posterior PDFs (profile likelihoods), and shading indicates 1 and 2 $\sigma$  credible (confidence) intervals. Crosses indicate the best fit, bullets the posterior mean, and red/yellow diamonds the true parameter values. (Ignore annotations referring to CMSSM and SUPERBAYES)

11. Upgraded FLATLIB to work with Pass 7 IRFs
12. Implemented the treatment of the diffuse BG and tested it in BG only simulations
13. Coupled DMBAYES to DIVER, a forthcoming differential evolution package from Roebber & Scott
14. Developed, implemented and tested the point source identification strategy

## 4 Internal history within the Fermi Collaboration

This analysis was proposed in October 2009, and an external author request for some of the involved parties approved (Roberto Trotta & Roberto Ruiz de Austri). Other external authors initially approved (Cumberbatch & Roszkowski) did not ultimately become involved. Pat's present status within the Collaboration is somewhat grey, so he may or may not require approval as an external author at a later stage.

Since October 2009, progress has been incremental but steady, with a small number of contributors extensively developing and testing the tools as time permitted. In mid 2010 the analysis reached a sufficiently mature stage for further development to be concretely discussed and carried out with others in the Collaboration; discussions and collaborative efforts began at this point with members of the Diffuse/Galprop group, leading to Gulli et al's involvement.

## 5 Some notes on specific parts of the code/analysis

### 5.1 Inference for general BR setup

As a first step a prior for the branching ratios had to be found. Instead of choosing a prior directly on the branching ratios it was decided to implement a log prior on the annihilation cross-sections. The branching ratios can be calculated from the cross-sections as

$$BR_{\chi\chi \rightarrow r_i r_i} = \frac{\sigma_{\chi\chi \rightarrow r_i r_i}}{\sum_j \sigma_{\chi\chi \rightarrow r_j r_j}} \quad (1)$$

The resulting effective prior on the branching ratios ensures that they add up to one.

The shape of this effective prior depends strongly on the prior range chosen for the log prior on the cross-sections. Three examples for the shape of the prior on the branching ratios in eight dimensions (i.e. for eight open annihilation channels) are shown in Fig. 3. From left to right the plots correspond to a log

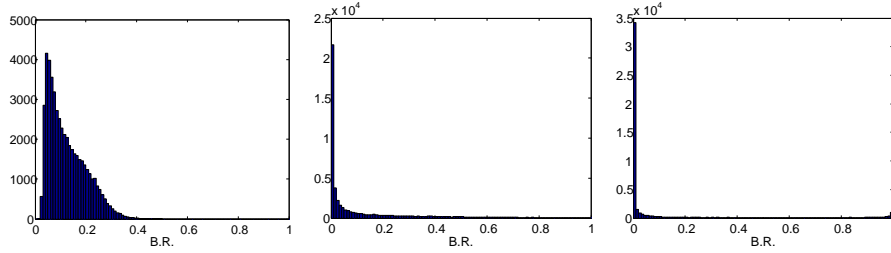


Figure 3: Shape of the effective prior on the branching ratios as a function of the range of the log prior on the cross-sections in eight dimensions. From top to bottom the range is equal to 1, 4 and 10.

prior range for the cross-sections of 1, 4 and 10. As can be seen, due to the high dimensionality small values of the BR are strongly favoured for the two larger ranges. This trend becomes less extreme when the number of open annihilation channels is reduced.

To investigate the influence of this choice of prior on the posterior distribution a scan of the parameter space was carried out assuming nine open annihilation channels, and imposing a log prior on the cross-sections with range  $[-2.0, 3.5]$ . A range of 5.5 was chosen, because for this range intermediate and high values of the BRs are equally well sampled by the prior. The true point is given by  $m_\chi = 167$  GeV,  $\log(\langle \sigma v \rangle \cdot 10^{+27} \text{cm}^3 \text{s}^{-1}) = 2.34$ ,  $BR_{b\bar{b}} = 0.844$ ,  $BR_{\tau^+\tau^-} = 0.156$ ,  $BR(\text{others}) \approx 0$ . The simulated data include background noise, based on public Galactic and isotropic background models. A scan with Bayesian set-up (Nested Sampling parameters  $n_{\text{live}} = 2000$ ,  $\text{tol} = 0.5$ ,  $\text{eff} = 0.3$ ) was carried out to reconstruct the DM parameters. The resulting plots of the profile likelihood and the marginalised posterior distribution are shown in Fig. 4. The WIMP mass and annihilation cross-section are reasonably well reconstructed, the true point is contained within the 2D 68% credible interval. However, the marginalised posterior distribution for the BRs is centred at very low values, far away from the true point. Likewise, the best fit point is also quite far away from the true point.

From the 1D posterior PDFs of the BRs (see Fig. 5) one can see that the posterior is strongly prior dominated: the shape of the 1D posteriors strongly resembles the shape of the prior distributions. Clearly the available data is not strong enough to overcome the impact of the prior. It can be concluded that while the posterior PDF can provide some information about the underlying parameter space, in most cases the impact of the prior will be too strong to allow for reliable parameter inference using the posterior PDF. Better results could be obtained from the profile likelihood distribution. For the Bayesian scan, the profile likelihood is not well-sampled around the true point, as can be

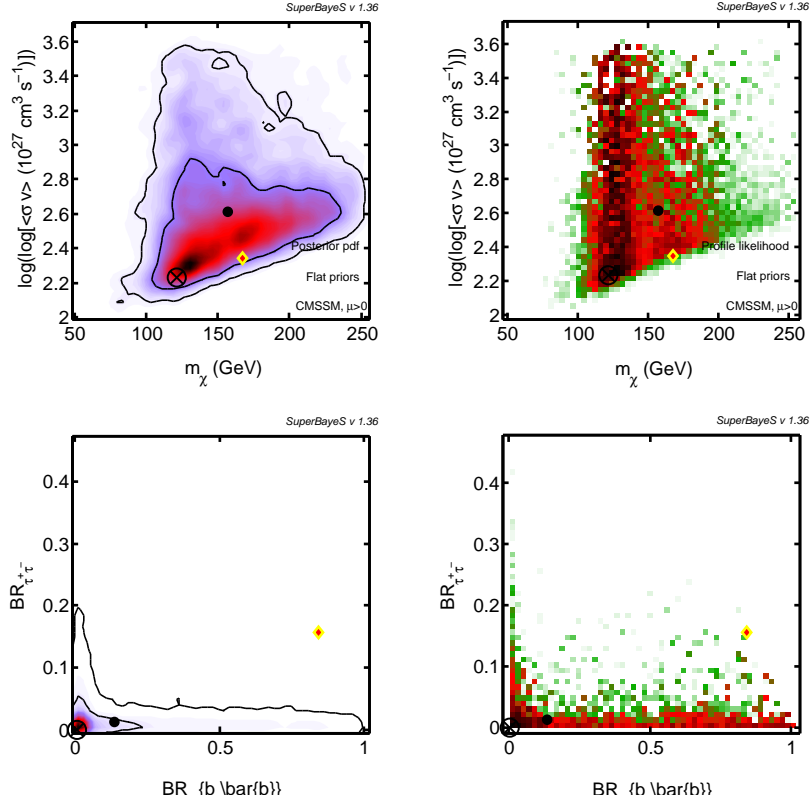


Figure 4: Parameter inference results from a scan with Bayesian set-up. The left (right) plots give marginalised posterior PDFs (profile likelihoods). Crosses indicate the best fit, bullets the posterior mean, and red/yellow diamonds the true parameter values. (Ignore annotations referring to CMSSM and SUPERBAYES)

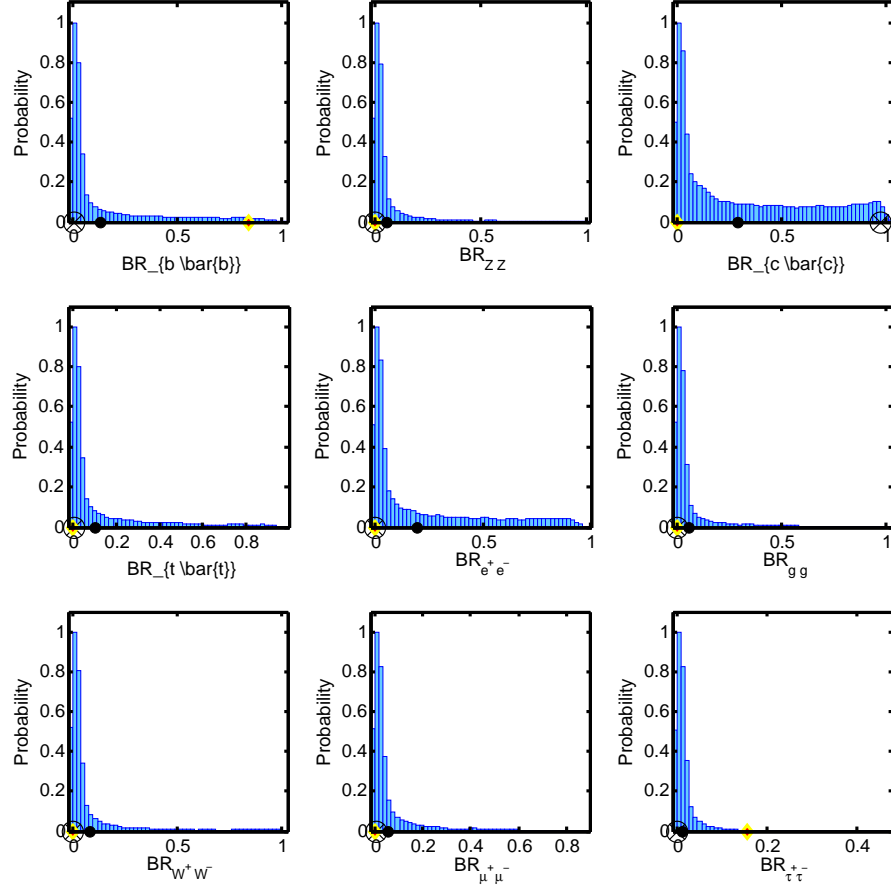


Figure 5: 1D marginalised posterior PDFs of the BRs resulting from a scan with Bayesian set-up. Crosses indicate the best fit, bullets the posterior mean, and red/yellow diamonds the true parameter values. (Ignore annotations referring to CMSSM and SUPERBAYES)



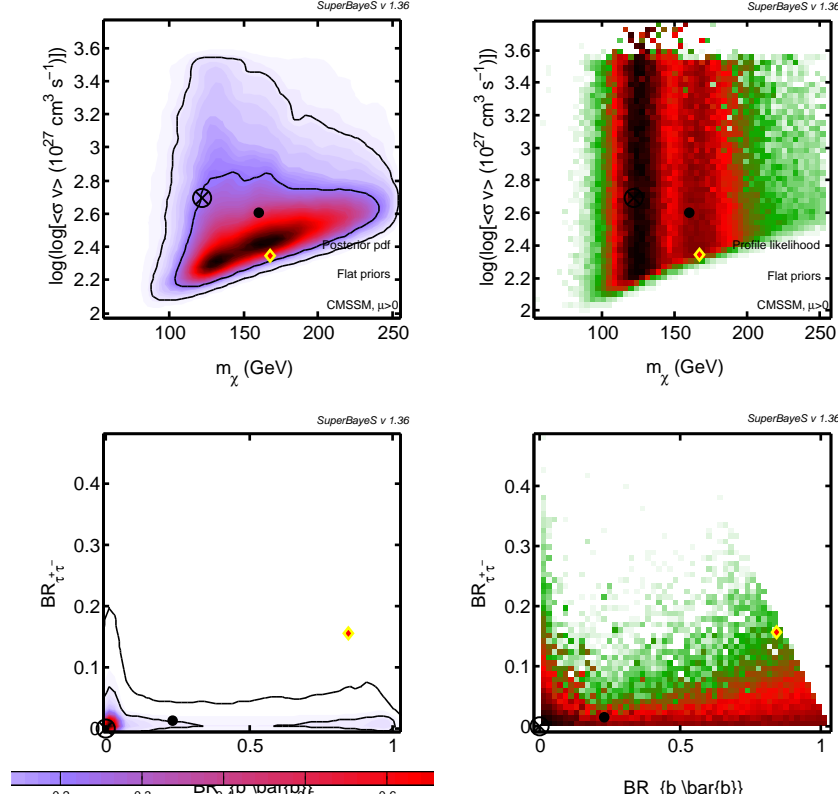


Figure 6: Parameter inference results from a scan with PL set-up. The left (right) plots give marginalised posterior PDFs (profile likelihoods). Crosses indicate the best fit, bullets the posterior mean, and red/yellow diamonds the true parameter values. (Ignore annotations referring to CMSSM and SUPERBAYES)

seen from the 2D profile likelihood plots. In order to obtain reliable results from the profile likelihood, the above scan was repeated for a PL set-up (MultiNest parameters  $n_{live} = 20000$ ,  $tol = 0.0001$ ,  $eff = 0.3$ ). The resulting plots of the 2D posterior PDFs and profile likelihoods are given in Fig. 6.

As can be seen, for a PL scan the parameter space around the true point is reasonably well sampled. The best fit point is still far away from the true point. This is most likely due to realisation noise in the simulated data. The posterior PDF is also still centred far away from the true point. To determine if the BRs are all reasonably well sampled within their allowed range  $[0,1]$  one can consider the 1D profile likelihood distributions, shown in Fig. 7.

As can be seen, the profile likelihood distributions cover most of the parameter space. In order to fully cover the range  $[0,1]$  for each of the BRs, the scan

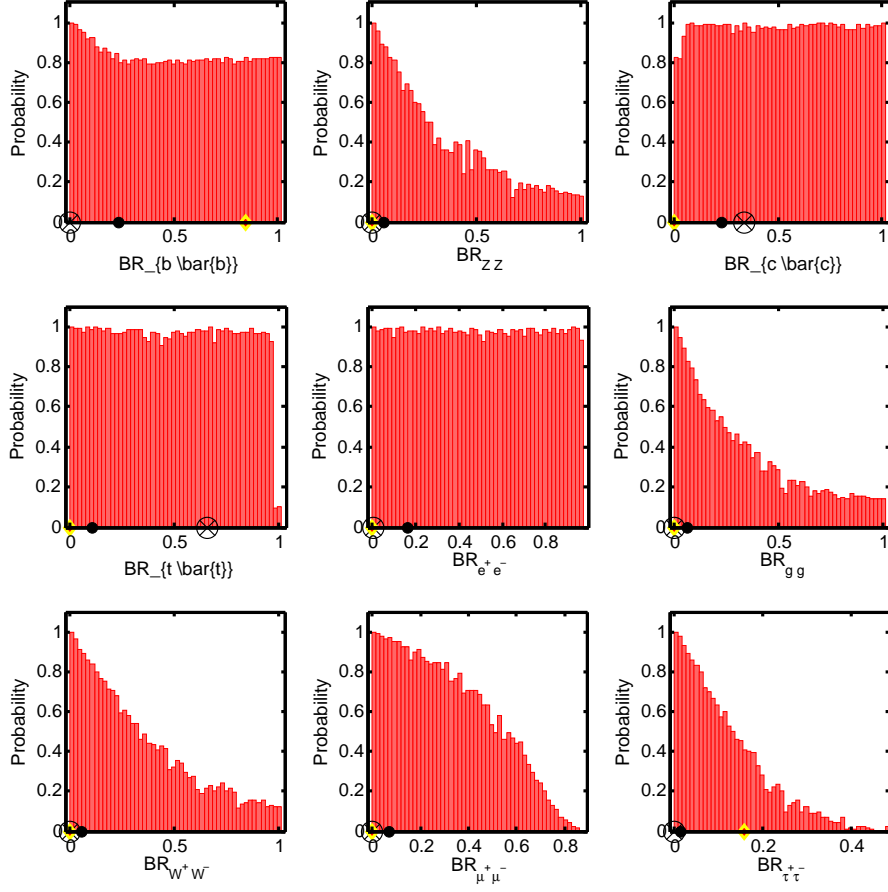


Figure 7: 1D profile likelihood functions of the BRs resulting from a scan with PL set-up. Crosses indicate the best fit, bullets the posterior mean, and red/yellow diamonds the true parameter values. (Ignore annotations referring to CMSSM and SUPERBAYES)

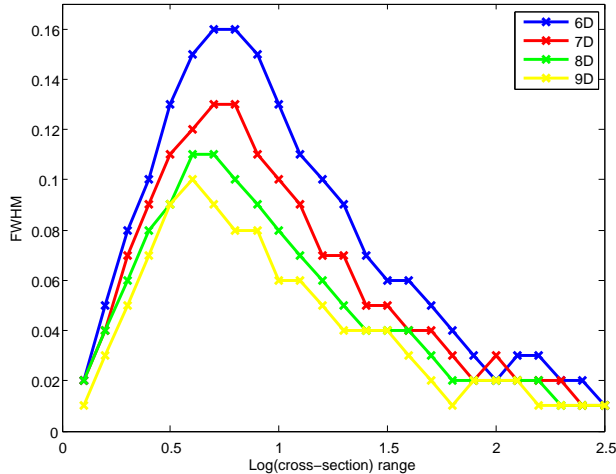


Figure 8: FWHM as a function of range of the log prior on the cross-sections for the effective prior on the BRs. The distribution is given for six (blue), seven (red), eight (green) and nine (yellow) dimensions.

will be repeated for three different effective priors and the resulting chains will be combined. The three priors will resemble the examples shown in Fig. 3. This will ensure that high, low and intermediate BR values are all well explored. The profile likelihood results from the combined chains can be used to infer the true values of the DM parameters.

The first effective prior on the BRs that will be used will have a similar shape as the distribution shown in the top plot in Fig. 3. This distribution corresponds to a small  $\log(\text{cross-section})$  range and will ensure that intermediate values of the BR are well-sampled. A useful quantity to investigate in order to determine which  $\log(\text{cross-section})$  range will lead to the best prior distribution to achieve this is the full width at half maximum (FWHM). The plot of the FWHM of the effective prior on the BRs as a function of the range of the log prior on the annihilation cross-sections is shown in in Fig. 8 for six, seven, eight and nine open annihilation channels. As a representative example, the data points in seven dimensions are given in table 1. The data in other dimensions show a similar behaviour.

Each of the curves in Fig. 8 have a similar shape, including a distinct peak. The higher the dimensionality of the parameter space, the the less pronounced is this peak. Additionally, the peak is shifted to slightly higher ranges as the dimensionality decreases. Given the shape of these distributions an obvious choice of effective prior for the BRs would be the distribution resulting from the log cross-section range at which the peak FWHM value is found. This is equivalent to maximising the number of bins containing a large number of points.

| $\text{Log}(\sigma_{\chi\chi \rightarrow r_i r_i})$ | Range | Largest Bin Position | # Non-zero Bins | FWHM |
|---|-------|----------------------|-----------------|------|
| 0.1   |       | 15                   | 5               | 0.02 |
| 0.2   |       | 14                   | 11              | 0.04 |
| 0.3   |       | 13                   | 16              | 0.07 |
| 0.4   |       | 12                   | 22              | 0.09 |
| 0.5   |       | 11                   | 27              | 0.11 |
| 0.6   |       | 10                   | 33              | 0.12 |
| 0.7   |       | 9                    | 39              | 0.13 |
| 0.8   |       | 8                    | 44              | 0.13 |
| 0.9   |       | 7                    | 50              | 0.11 |
| 1.0   |       | 6                    | 55              | 0.10 |
| 1.1   |       | 5                    | 61              | 0.09 |
| 1.2   |       | 5                    | 65              | 0.07 |
| 1.3   |       | 4                    | 70              | 0.07 |
| 1.4   |       | 4                    | 75              | 0.05 |
| 1.5   |       | 3                    | 78              | 0.05 |
| 1.6   |       | 3                    | 82              | 0.04 |
| 1.7   |       | 2                    | 85              | 0.04 |
| 1.8   |       | 2                    | 87              | 0.03 |
| 1.9   |       | 2                    | 89              | 0.02 |
| 2.0   |       | 2                    | 91              | 0.03 |
| 2.1   |       | 2                    | 93              | 0.02 |
| 2.2   |       | 2                    | 94              | 0.02 |
| 2.3   |       | 1                    | 95              | 0.02 |
| 2.4   |       | 1                    | 96              | 0.01 |
| 2.5   |       | 1                    | 97              | 0.01 |

Table 1: FWHM of the effective prior on the BRs in 7D for different ranges of the log prior on the cross-section. Additionally, the position of the largest bin and the number of non-zero bins is given for each range.

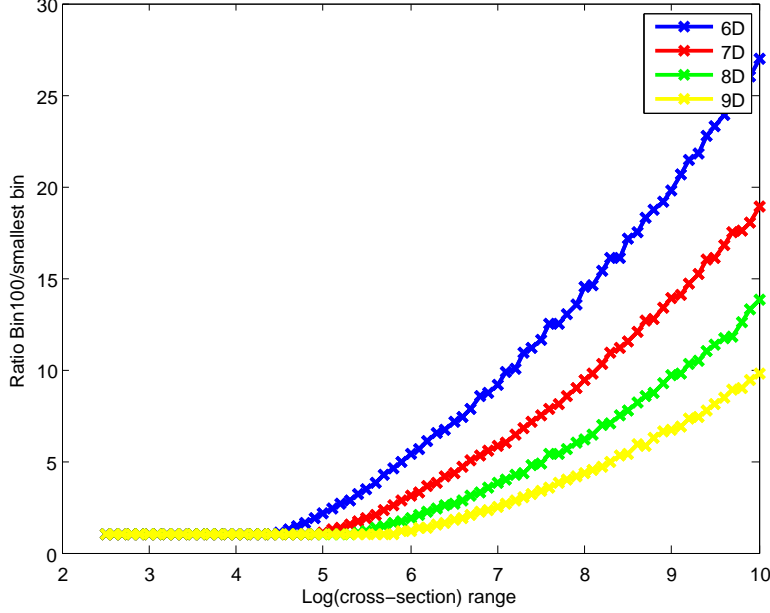


Figure 9: Ratio of the size of the last bin ( $BR = [0.99, 1.0]$ ) to the size of the smallest bin as a function of range of the log prior on the cross-sections for the effective prior on the BRs. The distribution is given for six (blue), seven (red), eight (green) and nine (yellow) dimensions.

However, it is important to keep in mind that both smaller and larger ranges for the log prior on the cross-sections have certain advantages. As can be seen in Table 1, the smaller the range, the more central is the position of the largest bin. Therefore, while the distribution does become narrower for smaller ranges, more central values of the BRs may be better sampled. On the other hand, the larger the range, the larger the number of bins that contain a non-zero number of points. Therefore, the overall number of BR values sampled increases, even though they might not be sampled as well as for smaller cross-section ranges.

The second effective prior on the BRs that is of interest resembles the shape of the distribution shown in the central plot of Fig. 3. This prior distribution would lead to intermediate and large BR values being equally well sampled. To investigate which range for the log prior on the cross-section to choose to obtain this effective prior one can consider the ratio of the size of the last bin ( $BR = [0.99, 1.0]$ ) to the size of the smallest bin. This ratio is shown in Fig. 9 as a function of the range of the log prior on the cross-sections for different dimensionalities of the parameter space. As can be seen, this ratio is equal to unity for small ranges, since for these ranges the last bin and the the smallest

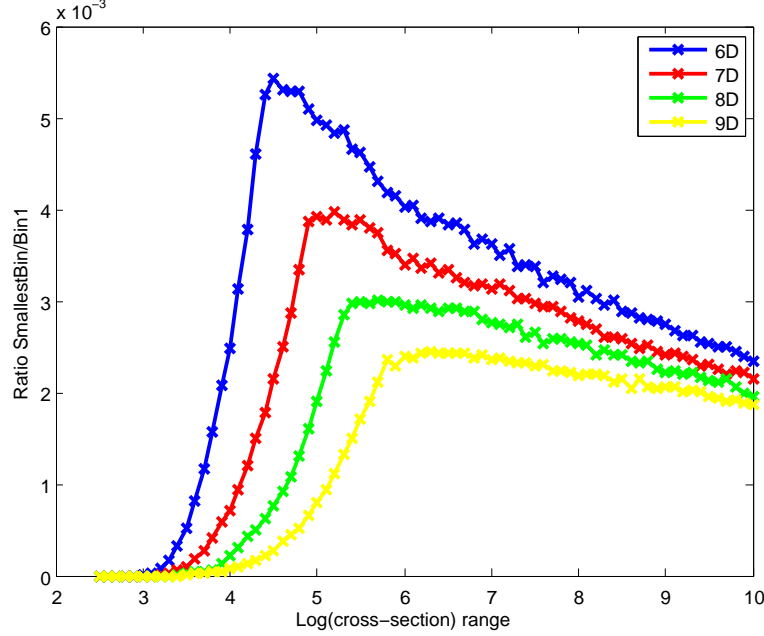


Figure 10: Ratio of the size of the smallest bin to the size of the first bin ( $\text{BR} = [0.0, 0.01]$ ) as a function of range of the log prior on the cross-sections for the effective prior on the BRs. The distribution is given for six (blue), seven (red), eight (green) and nine (yellow) dimensions.

bin are identical. At some range the ratio becomes larger than unity, because the size of the last bin is now larger than the size of the smallest bin. As can be seen, the larger the number of free BRs, the larger the range of the log prior on the annihilation cross-sections at which this ratio becomes greater than unity.

Another interesting quantity to consider in order to determine which range leads to the best sampling of the parameter space is the ratio of the size of the smallest bin to the size of the first bin ( $\text{BR} = [0.0, 0.01]$ ). In Fig. 10 this ratio is shown as a function of the range of the log prior on the annihilation cross-sections for different numbers of free BRs. The distribution is peaked around a certain range value, which shifts towards higher ranges as the dimensionality of the parameter space increases. By comparing Fig. 10 and Fig. 9 one can see that the peak occurs at similar (slightly higher) ranges as the range at which the smallest bin position starts to move towards more central values of the BRs. Therefore, a good choice of effective prior for the BRs in each dimension would be the distribution resulting from the range of the log prior on the cross-sections at which the peak of the ratio of size of the smallest bin to the size of the first bin is found.

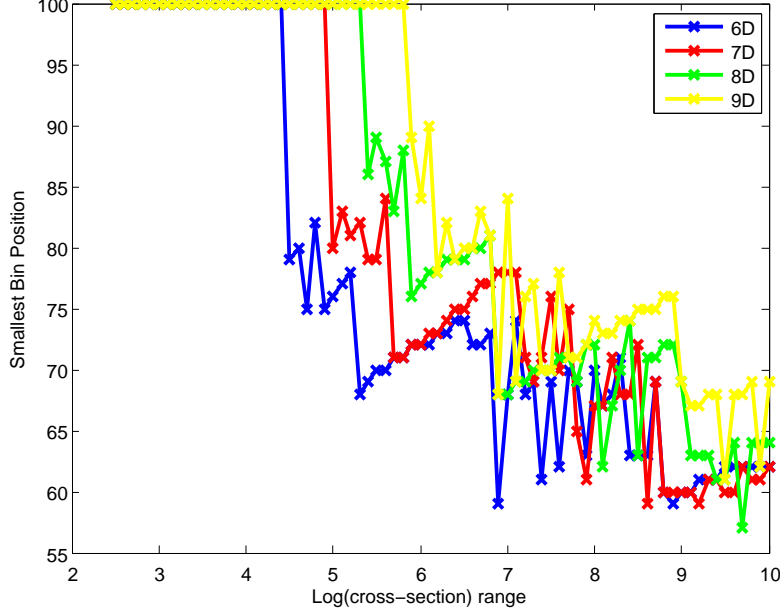


Figure 11: Position of the smallest bin as a function of range of the log prior on the cross-sections for the effective prior on the BRs. The distribution is given for six (blue), seven (red), eight (green) and nine (yellow) dimensions.

When trying to choose the most convenient such prior by using ratios involving the size of the smallest bin, it is useful to keep track of the position of this bin. This position as a function of range of the log prior on the cross-sections can be seen in Fig. 11. Even though there is a relatively large scatter in the position of the smallest bin as a function of range, one can clearly see that the position of the smallest bin shifts towards more central values of the BRs as the range of the log prior on the annihilation cross-sections increases.

The third type of prior that we want to use will resemble the shape of the distribution shown in the bottom plot in Fig. 3. Such a distribution corresponds to an effective prior on the BRs that will mostly sample extreme values of the BRs, i.e. both very high or very low values. In order to choose a range of the log prior on the cross-sections leading to such a distribution one can consider the ratio of the size of the last bin ( $\text{BR} = [0.99, 1.0]$ ) to the size of the first bin ( $\text{BR} = [0.0, 0.01]$ ). The plot of this ratio as a function of the range of the log prior on the annihilation cross-sections is given in Fig. 12 for different dimensionalities of the parameter space. As can be seen, this ratio is zero for small ranges, since the last bin does not contain any points. The range at which this ratio becomes non-zero increases as the number of free BRs increases. Once the ratio is non-zero it

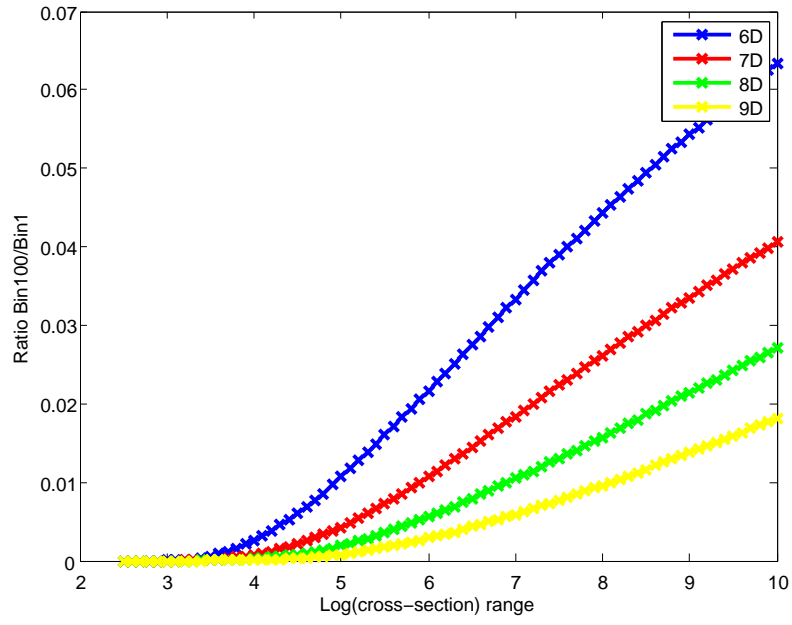


Figure 12: Ratio of the size of the last bin ( $BR = [0.99, 1.0]$ ) to the size of the first bin ( $BR = [0.0, 0.01]$ ) for the effective prior distribution on the BRs as a function of range of the log prior on the cross-sections. The distribution is given for six (blue), seven (red), eight (green) and nine (yellow) dimensions.



steadily grows with the range of the log prior on the cross-sections. Therefore, the higher the range, the better sampled are high values of the BRs. However, one should keep in mind that the larger the range, the more the distribution is concentrated at very low and very high values of the BRs, and thus the smaller the number of bins that are well-sampled.

**CS: The most important questions are:**

- **Small range prior:** Should we use the distribution resulting from the log cross-section range at which the peak FWHM value is found? Smaller ranges would lead to a more central position of the largest bin, but would also lead to a smaller BR range being sampled. Larger ranges would lead to a larger sampled BR range, but the number of bins with a high number of points decreases and the maximum of the distribution is shifted to lower values of the BRs.
- **Medium range prior:** I recommend using the distribution resulting from the range of the log prior on the cross-sections at which the peak of the ratio of size of the smallest bin to the size of the first bin is found as the second effective prior for the BRs. What do other people think?
- **Large range prior:** Which range of the log prior on the cross-sections should we choose for the third type of prior? The higher the range, the better very high values of the BRs are sampled (the larger the ratio of the size of the last bin to the size of the first bin). However, the larger the range, the smaller the number of bins that is well-sampled. What is a good criterion to choose the range for this prior?

## 5.2 Background modelling

### 5.2.1 Set-up

The background models depend non-linearly on some parameters, whereas the dependence on others can be approximated by a linear or power-law scaling. For the non-linear parameters (**grid parameters**), we generated a grid of mapcubes that covers reasonable variations of the background model with these parameters. Each grid point has a set of template maps associated with it, each representing a contribution to the total flux. Each template map is rescaled by the appropriate linear/power-law parameters (**template parameters**), then the 14 rescaled template maps are added together to give the total flux for the considered grid point. The correct flux map for every point in parameter space can be found by **linear interpolation** between the grid points. A typical interpolation within this two-step model happens as follows:

1. Choose a specific combination of grid parameters  $\theta_g$ , and a specific combination of template parameters  $\theta_t$  (i.e. a single point in the full  $(1 + 10)$ D background parameter space).
2. Identify the points in the grid defining the hypercube surrounding  $\theta_g$ .
3. For all vertices of that hypercube, use  $\theta_t$  to compute the scaled template contributions to the total background model at each vertex.
4. At each vertex, add the fluxes of the respective template contributions to obtain the total background model at that vertex.
5. Linearly interpolate the resulting total background maps from these vertices to the chosen point in the grid  $\theta_g$ .

We have decided on a spatial pixel size of  $0.25 \times 0.25$  degrees, 15 log-spaced energy bins from 300 MeV to 100 GeV, and a  $15 \times 15$  degrees ROI for PSF convolution – of which a  $10 \times 10$  degree region will be used for the likelihood calculation.

### 5.2.2 Detailed description of the background model parameters

In its simplest form, the ISM background model is a line of sight integral of the product of target density and CR density. Unfortunately, neither is known with great accuracy.

#### Target distributions

The two big contributors in the ISM are hydrogen and helium gas. Cold helium cannot be observed so it is usually assumed to have the same distribution as hydrogen. Hydrogen in the ISM has three forms: atomic, molecular, and ionised. Atomic hydrogen is observed with the 21-cm hyperfine line that has to be corrected for optical depth. That is done using the spin temperature  $T_S$  under the assumption of uniform  $T_S$  along the line of sight (for that particular Doppler shift of the 21-cm line). The HI column density is given with

$$N(HI) = -\log \left( 1 - \frac{T}{T_S - T_{bg}} \right) T_S C \quad (2)$$

where  $T$  is the line temperature,  $C = 1.83 \times 10^{18} \text{ cm}^{-2} \text{ K (km/s)}^{-1}$ , and  $T_{bg}$  is the background temperature, usually assumed to be the CMB background. For  $T_S \rightarrow \infty$  we have  $N(HI) \propto T$  while when  $T_S \rightarrow T + T_{bg}$  we have  $N(HI) \rightarrow \infty$ . To have a more linear parameter in the grid, we actually scan over

$$x_S \equiv \left( \frac{T_S}{K} \right) \log_{10} \left[ 1 - \left( \frac{80K}{T_S} \right) \right], \quad (3)$$

instead of  $T_S$  itself.

The molecular hydrogen is not directly observed so we use CO maps as a proxy for the  $H_2$  distribution. We use a linear approximation to turn integrated CO line intensity,  $W(CO)$ , into column density  $N(H_2) = X_{CO}W(CO)$ . There is some evidence that  $X_{CO}$  is variable over the Galaxy and this is especially true close to the GC.

We use the Doppler shift of the lines to place the gas along the line of sight assuming the gas is rotating around the GC. This method breaks down close to the GC (within  $\sim 10^\circ$ ) and we use linear interpolation from surrounding areas. The distribution of gas is therefore highly uncertain in the ROI.

### CR distribution

The distribution of CRs depends on the distribution of sources and their propagation throughout the Galaxy. To simplify things, we assume we know the propagation and only adjust the source distribution. This is of course a simplification, but should suffice to parameterise the uncertainty of the background model. We go a step further and adjust the propagated CR flux with a functional form

$$CR(R) \propto \left(\frac{R}{R_\odot}\right)^\alpha e^{-\beta \frac{R-R_\odot}{R_\odot}} \quad (4)$$

We'll start by changing only  $\alpha$  with a fixed  $\beta$ , basically controlling the peakiness of the CR source distribution. The lower the value of  $\alpha$ , the peakier the distribution gets. We use the same distribution for the CR sources as in GALPROP. The distribution of CRs is supposed to include uncertainty in the distribution of targets as well. Due to our limited source distribution function, this might not be accurate.

### Some approximations we apply

To make the runs simpler, we do not include secondary electrons and positrons. They mostly affect the ISM model at low energies and we are anyway focused on the DM limits, not the background model. Since they are generated from CR protons, we would have to split the electron components into secondary and primary components and add them to the proton component. This can be done but introduces more parameters (and work).

To simplify things we change the spectral index of the final products rather than the injected CRs. This is accurate when the propagation only changes the power law index of the injected spectrum, which holds pretty well in the energy range from a few GeV to few hundred GeV for electrons and few TeV for protons. This is in fact the energy range we are considering for this analysis so it should be safe. Note that when we change the spectrum we have to allow for freedom in the normalisation as well, that is we multiply the templates with  $f(E) = f_0 * E^i$  where  $f_0$  and  $i$  are free parameters.

### 5.2.3 Specifics of particular grid setups

#### Test Grid I

The directory `bg_data` contains a subfolder `TestGridI`. This folder contains the test grid. This folder contains one subfolder for each grid point corresponding to different values of the grid parameter(s), which contains the template .fits files for the grid point. `TestGridI` also contains an index file; the location of the index file for a scan will be given in the .ini file. The index file contains information about the number of grid and template parameters, the number of templates and the parameter names. It also contains the values of the grid parameters associated with each grid point, the type of template parameter (linear or special), and the templates rescaled by each template parameter. In order to implement the BG parameters in the code two new parameter types (`Grid_params`, `Template_params`) were defined.

The following model currently stored in `TestGridI`:

*Grid parameters:*

- Spin temperature,  $T_S$

*Template parameters:*

- CR proton source distribution ( $\alpha$ , and/or  $\beta$ )
- CR proton spectra index and normalisation
- CR electron spectral index and normalisation
- $X_{CO}$  parameters, one for each of 0–1.5 kpc, 1.5–3 kpc, 3–50 kpc

There are 6 values of  $T_S$  for this model so only 6 grid points. The templates for each grid point is stored in a separate directory, called `TestGridI_<i>`, where *i* is a grid index going from 1 to 6. Each of the template map cubes has 0.25 degree pixel resolution and spans [-15,15] degrees. The mapping to  $T_S$  (and  $x_S$ ) values is as follows:

| Grid index | $T_S$ [K] | $x_S$ |
|------------|-----------|-------|
| 1          | 100       | -69.9 |
| 2          | 125       | -55.5 |
| 3          | 150       | -49.6 |
| 4          | 200       | -44.4 |
| 5          | 400       | -38.8 |
| 6          | 100000    | -34.8 |

Each grid point has 13 template maps associated with it, created by summing up various GALPROP output components. There is also one additional template map, identical at each grid point, associated with the Fermi bubbles. **PS: This 14th template still needs to be added.** The template filenames are `TestGridI_<i>_<j>`, where *j* is a template index going from 1 to 13. The mapping between templates and the index is:

| Template index | Description                                      |
|----------------|--|
| 1              | Bremss for HI and HII and ics                    |
| 2              | Bremss for H <sub>2</sub> from 0–1.5 kpc         |
| 3              | Bremss for H <sub>2</sub> from 1.5–3 kpc         |
| 4              | Bremss for H <sub>2</sub> from 3–30 kpc          |
| 5              | $\pi^0$ -decay for HI an HII from 0–3 kpc        |
| 6              | $\pi^0$ -decay for HI an HII from 3–5 kpc        |
| 7              | $\pi^0$ -decay for HI an HII from 5–10 kpc       |
| 8              | $\pi^0$ -decay for HI an HII from 10–30 kpc      |
| 9              | $\pi^0$ -decay for H <sub>2</sub> from 0–1.5 kpc |
| 10             | $\pi^0$ -decay for H <sub>2</sub> from 1.5–3 kpc |
| 11             | $\pi^0$ -decay for H <sub>2</sub> from 3–5 kpc   |
| 12             | $\pi^0$ -decay for H <sub>2</sub> from 5–10 kpc  |
| 13             | $\pi^0$ -decay for H <sub>2</sub> from 10–30 kpc |
| 14             | Fermi bubbles                                    |

Templates 1–4 should be multiplied with the CR electron spectral index (correction) and normalization. Templates 2–4 should be multiplied with  $X_{CO}$  factors, one factor for each template. The same  $X_{CO}$  factors should be applied to templates 9–13, where the same  $X_{CO}$  factor is used for templates 11–13. Templates 5–13 should be multiplied with the CR proton spectra index and normalization. These templates should also be corrected for the proton CR source distribution. We pick a reference  $R$  value for each template to calculate the normalization (**AR:  $E_0 = 3.405$  GeV,  $R_0 = 8.5$  kpc in fermi\_ini.f90::GC\_BG\_rescaled**).

| Template multiplied by rescaling factor | rescaling factor   |
|---|--|
| 1-4                                     | $\left(\frac{E_{center}}{E_0}\right)^{index_e}$  |
| 1-4                                     | $norm_e$   |
| 2,9                                     | $X_{CO,1}$   |
| 3,10                                    | $X_{CO,2}$   |
| 4,11,12,13                              | $X_{CO,3}$   |
| 5-13                                    | $norm_p$   |
| 5-13                                    | $\left(\frac{E_{center}}{E_0}\right)^{index_p}$  |
| 5-13                                    | $\frac{(R/R_0)^\alpha \cdot \exp(-\beta(R-R_0)/R_0)}{(R/R_0)^2 \cdot \exp(-5(R-R_0)/R_0)}$ |

As an example, the 13 template maps associated with grid point 3 are given in Fig. 13 - 25. For each template map two plots are shown. The left-hand plot corresponds to the first (lowest) energy bin, the right-hand plot corresponds to the last (highest) energy bin.

The minimum and maximum flux values corresponding to each template map are given in the caption. By comparing these numbers the contributions of different templates to the total flux can be estimated.

The BG parameters, their parameter type and their prior ranges are given in table 2. Template parameters are classified according to their rescaling properties. Linear template parameters rescale one or more of the templates in a

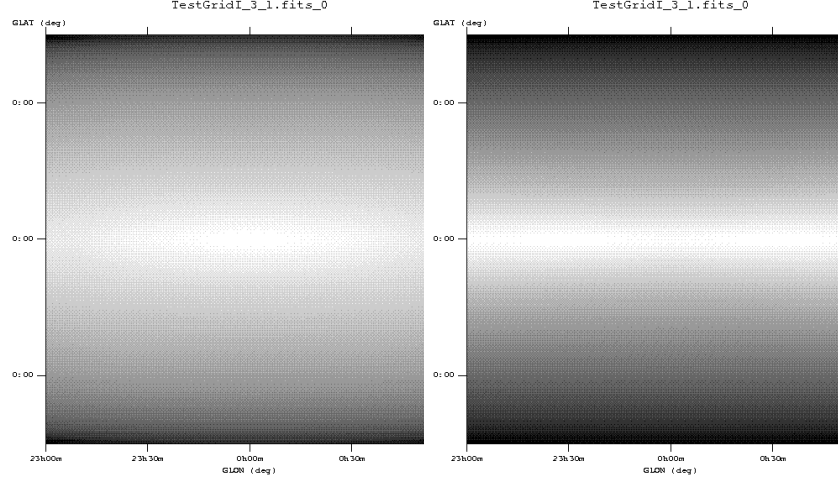


Figure 13: Template 1 flux maps for the first (left) and last (right) energy bin. The flux range is  $\text{flux} = [6.75 \cdot 10^{-7}, 4.41 \cdot 10^{-6}]$  ( $\text{flux} = [5.13 \cdot 10^{-18}, 1.21 \cdot 10^{-16}]$ ) in the first (last) energy bin.

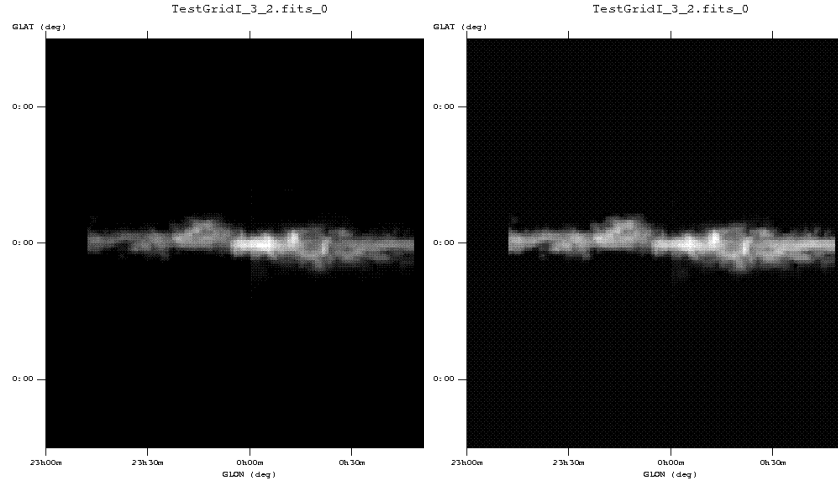


Figure 14: Template 2 flux maps for the first (left) and last (right) energy bin. The flux range is  $\text{flux} = [-9.47 \cdot 10^{-9}, 5.58 \cdot 10^{-5}]$  ( $\text{flux} = [-7.30 \cdot 10^{-21}, 1.35 \cdot 10^{-17}]$ ) in the first (last) energy bin.

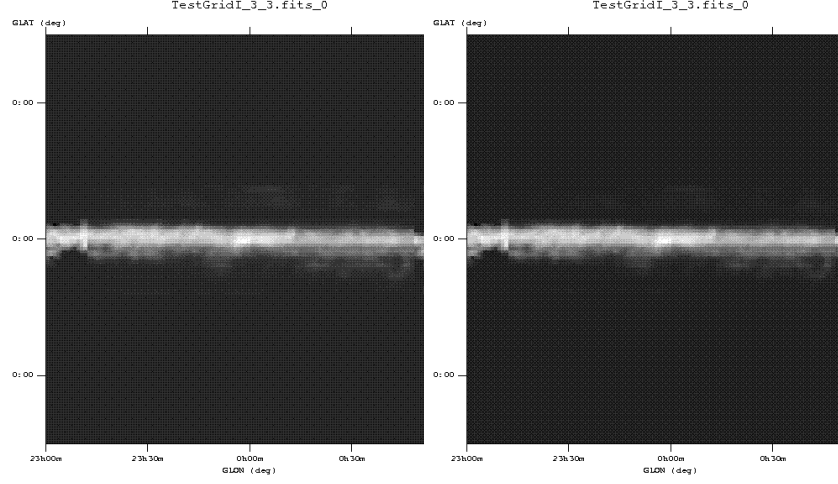


Figure 15: Template 3 flux maps for the first (left) and last (right) energy bin. The flux range is  $\text{flux} = [-2.06 \cdot 10^{-8}, 3.83 \cdot 10^{-6}]$  ( $\text{flux} = [-2.38 \cdot 10^{-20}, 5.45 \cdot 10^{-18}]$ ) in the first (last) energy bin.

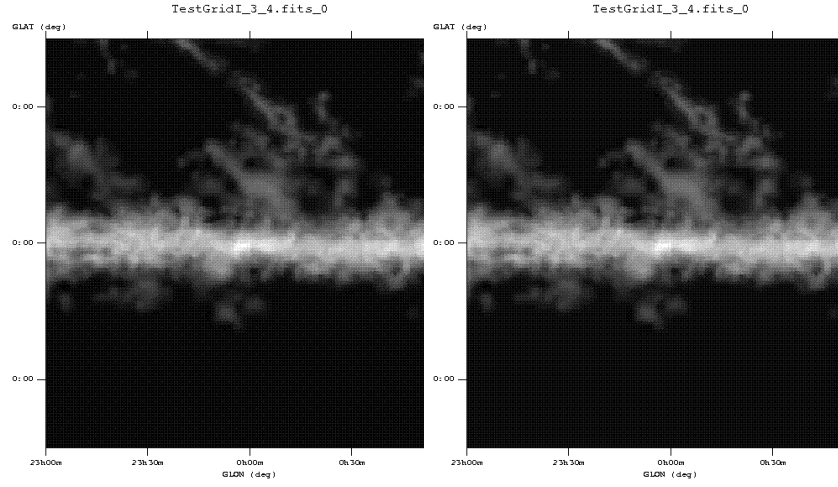


Figure 16: Template 4 flux maps for the first (left) and last (right) energy bin. The flux range is  $\text{flux} = [-1.43 \cdot 10^{-8}, 1.34 \cdot 10^{-5}]$  ( $\text{flux} = [-3.66 \cdot 10^{-20}, 2.96 \cdot 10^{-17}]$ ) in the first (last) energy bin.

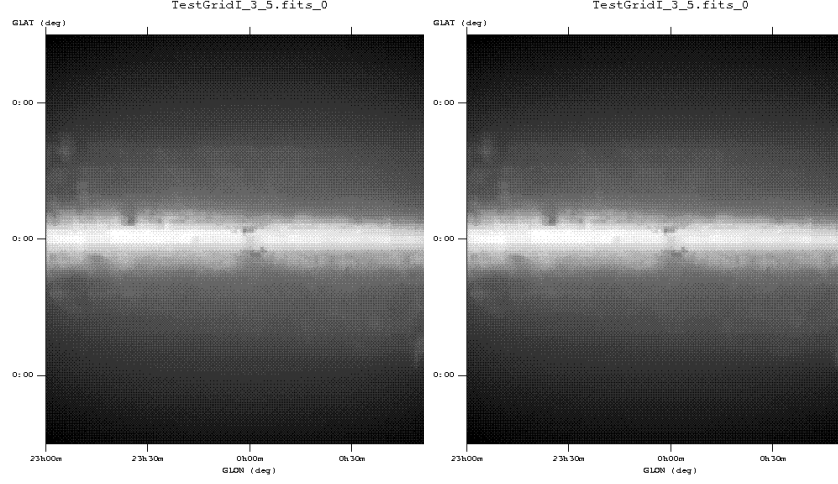


Figure 17: Template 5 flux maps for the first (left) and last (right) energy bin. The flux range is  $\text{flux} = [1.01 \cdot 10^{-8}, 2.08 \cdot 10^{-6}]$  ( $\text{flux} = [8.43 \cdot 10^{-19}, 2.15 \cdot 10^{-16}]$ ) in the first (last) energy bin.

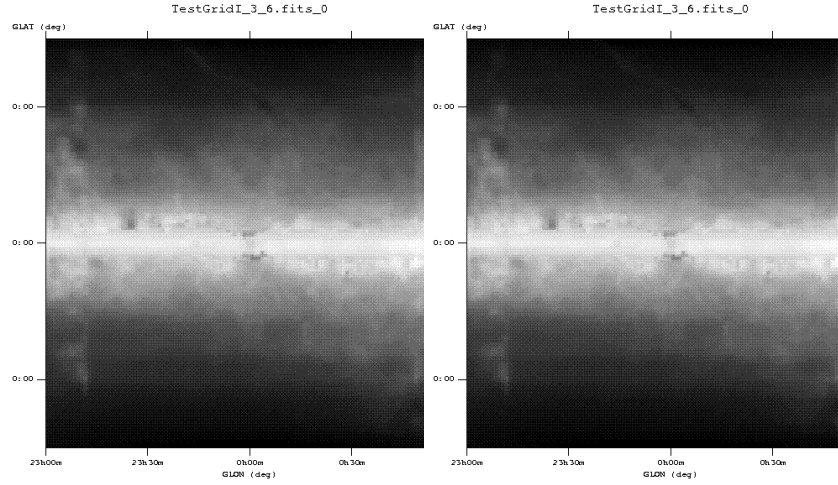


Figure 18: Template 6 flux maps for the first (left) and last (right) energy bin. The flux range is  $\text{flux} = [1.13 \cdot 10^{-8}, 2.13 \cdot 10^{-6}]$  ( $\text{flux} = [1.08 \cdot 10^{-18}, 2.42 \cdot 10^{-16}]$ ) in the first (last) energy bin.



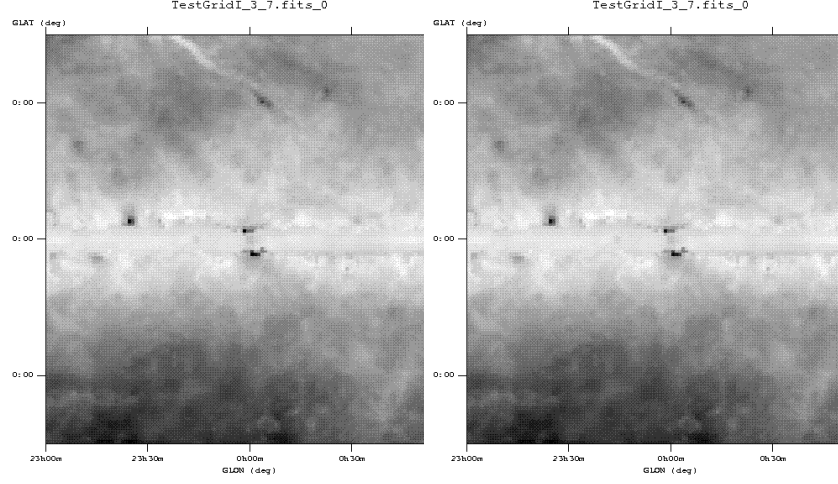


Figure 19: Template 7 flux maps for the first (left) and last (right) energy bin. The flux range is  $\text{flux} = [1.02 \cdot 10^{-7}, 3.67 \cdot 10^{-6}]$  ( $\text{flux} = [1.07 \cdot 10^{-17}, 4.04 \cdot 10^{-16}]$ ) in the first (last) energy bin.

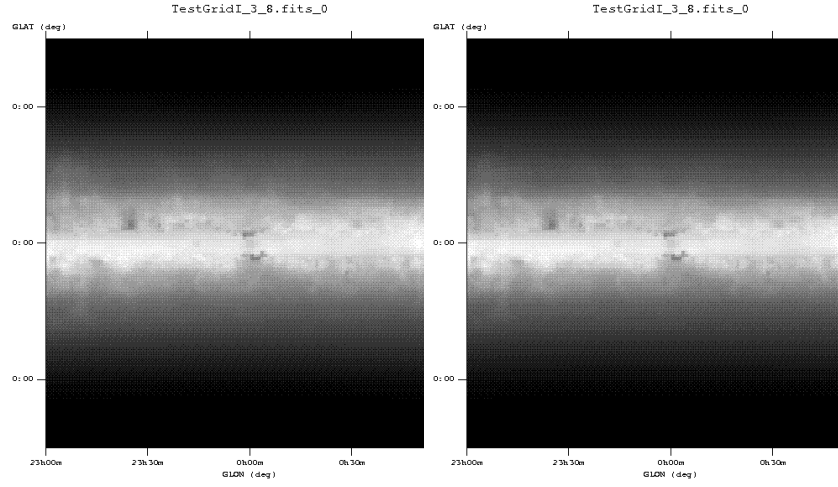


Figure 20: Template 8 flux maps for the first (left) and last (right) energy bin. The flux range is  $\text{flux} = [-2.04 \cdot 10^{-15}, 2.00 \cdot 10^{-7}]$  ( $\text{flux} = [-1.49 \cdot 10^{-25}, 1.68 \cdot 10^{-17}]$ ) in the first (last) energy bin.

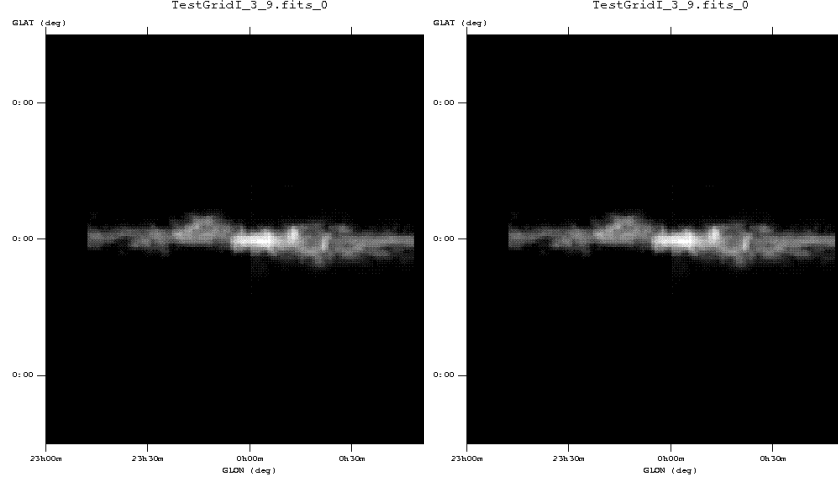


Figure 21: Template 9 flux maps for the first (left) and last (right) energy bin. The flux range is  $\text{flux} = [-2.12 \cdot 10^{-8}, 1.4 \cdot 10^{-4}]$  ( $\text{flux} = [-2.10 \cdot 10^{-18}, 1.28 \cdot 10^{-14}]$ ) in the first (last) energy bin.

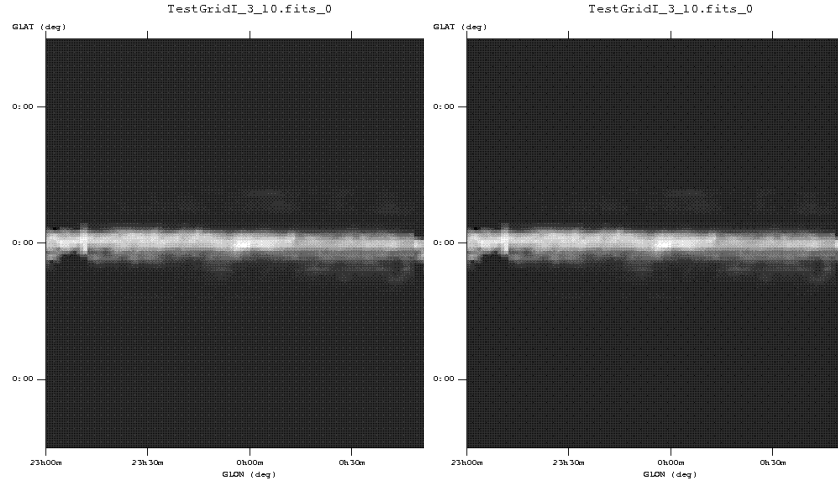


Figure 22: Template 10 flux maps for the first (left) and last (right) energy bin. The flux range is  $\text{flux} = [-4.53 \cdot 10^{-8}, 8.38 \cdot 10^{-6}]$  ( $\text{flux} = [-4.74 \cdot 10^{-18}, 8.95 \cdot 10^{-16}]$ ) in the first (last) energy bin.

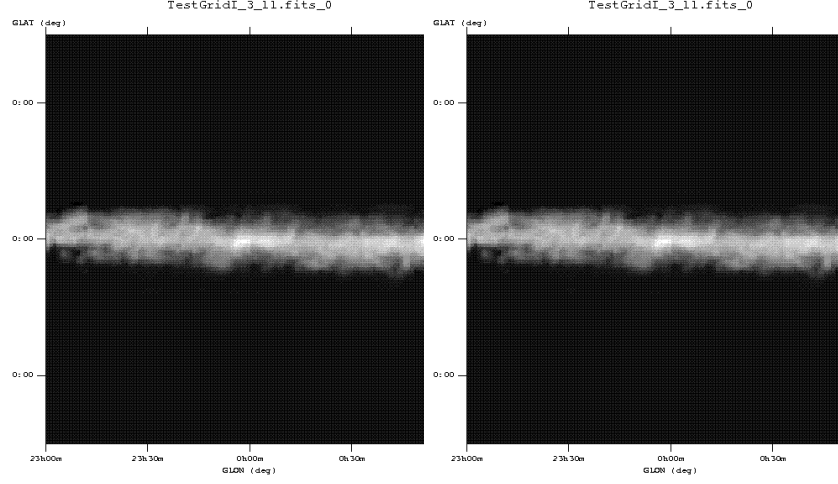


Figure 23: Template 11 flux maps for the first (left) and last (right) energy bin. The flux range is  $\text{flux} = [-2.81 \cdot 10^{-8}, 1.58 \cdot 10^{-5}]$  ( $\text{flux} = [-3.16 \cdot 10^{-18}, 1.80 \cdot 10^{-15}]$ ) in the first (last) energy bin.

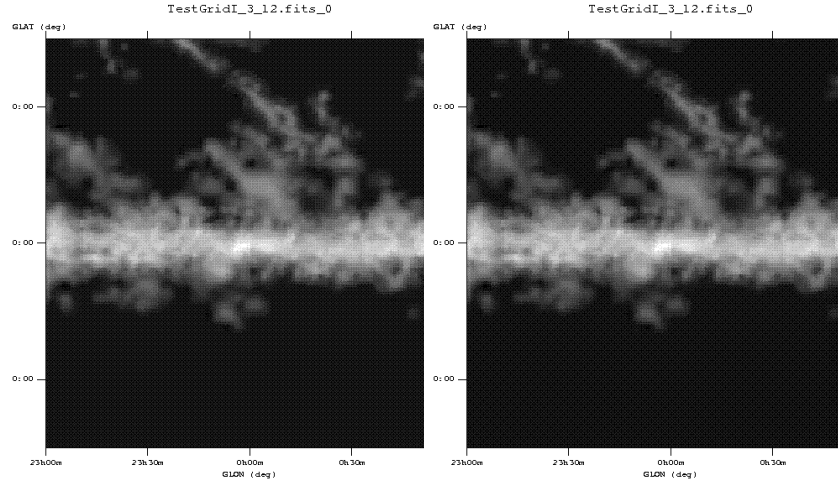


Figure 24: Template 12 flux maps for the first (left) and last (right) energy bin. The flux range is  $\text{flux} = [-3.59 \cdot 10^{-8}, 1.53 \cdot 10^{-5}]$  ( $\text{flux} = [-3.75 \cdot 10^{-18}, 1.73 \cdot 10^{-15}]$ ) in the first (last) energy bin.

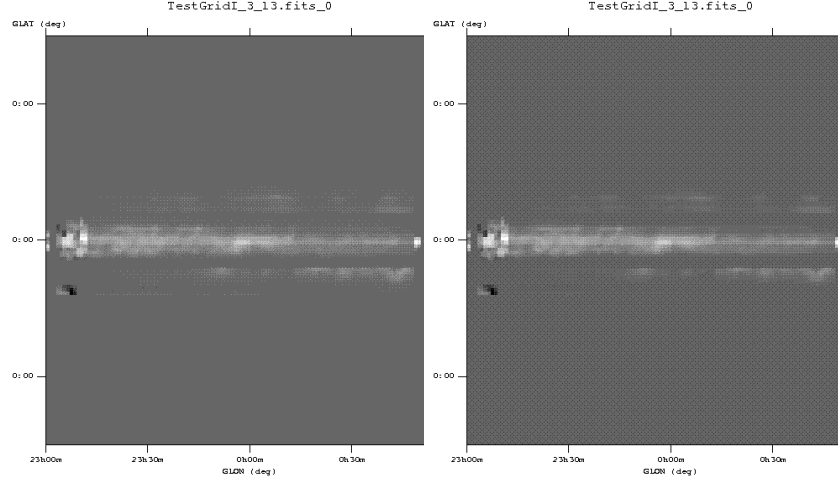


Figure 25: Template 13 flux maps for the first (left) and last (right) energy bin. The flux range is  $\text{flux} = [-1.41 \cdot 10^{-9}, 4.22 \cdot 10^{-8}]$  ( $\text{flux} = [-1.10 \cdot 10^{-19}, 3.80 \cdot 10^{-18}]$ ) in the first (last) energy bin.

linear fashion. Special parameters are parameters with more complicated scaling properties. We deal with one grid parameter, six linear parameters and four special (i.e. nonlinear) parameters. The nonlinear parameters are the CR proton and electron spectral indices and source distribution parameters  $\alpha$  and  $\beta$ . The full set of parameters is given in Table 2.

| Parameter     | Parameter Type     | Prior Range                 |
|---------------|--------------------|-----------------------------|
| $T_S(x_S)$    | Grid               | [100,100000]([-69.9,-34.8]) |
| $X_{CO}(1)$   | Template (Linear)  | [0.1,5.0]                   |
| $X_{CO}(2)$   | Template (Linear)  | [0.1,5.0]                   |
| $X_{CO}(3)$   | Template (Linear)  | [0.1,5.0]                   |
| index(e)      | Template (Special) | [-0.3,0.3]                  |
| norm(e)       | Template (Linear)  | [0.1,10.0]                  |
| index(p)      | Template (Special) | [-0.3,0.3]                  |
| norm(p)       | Template (Linear)  | [0.1,10.0]                  |
| $\alpha$      | Template (Special) | [1.0,5.0]                   |
| $\beta$       | Template (Special) | [3.0,10.0]                  |
| norm(bubbles) | Template (linear)  | [0.1,10.0]                  |

Table 2: Background parameters their parameter type (grid or template; if template linear or special rescaling) and their prior ranges.

## 5.3 Point source fitting methodology

### 5.3.1 Spectral model

There are different spectra one can use (straight power law, log parabola, exponential cutoff power law). To be able to fit every source at least as well as in the official Fermi point source catalogue, we decided to use a combination of these possible spectra. This combination is a log parabola with an exponential cutoff:

$$\frac{dN}{dE} = N_0 \left( \frac{E}{E_0} \right)^{-[\alpha + \beta \log(E/E_0)]} e^{-(E-E_0)/E_c}.$$

This results in a set of five parameters for the spectrum of a point source  $\Theta_{\text{spec}} = \{N_0, E_0, E_c, \alpha, \beta\}$ , plus two for the position of the source on the sky  $\Theta_{\text{pos}} = l, b$ .

### 5.3.2 Source identification

In order to identify the point sources we use Bayesian object detection, following Feroz & Hobson (2008). During the analysis it is assumed that only one point source is present in some background noise, so that we only have to scan over the parameters for a single point source (+ background parameters). The posterior distribution found by MultiNest has several peaks, each (potentially) corresponding to a different point source. By evaluating the local Bayesian evidence of these peaks and comparing them to the global null evidence (the evidence assuming that there is no point source in the image) one can determine if the peak in the posterior does indeed correspond to a point source. That is, we use Bayesian model selection to distinguish between

- $H_0$ : the detected object is fake (amplitude = 0, or alternatively amplitude  $< A_{\text{lim}}$ )
- $H_1$ : the detected object is real (amplitude  $> 0$ , or alternatively amplitude  $> A_{\text{lim}}$ ).

This method was shown to work for signal-to-noise ratios of 0.5 - 1.0.

Note that this approach is known to not work well for separating out two objects that lie very close together and have very different amplitudes. The other problems when applying this approach to the Fermi GC analysis is that by assuming that only one point source is present in the ROI one will automatically overestimate the background (which then receives contributions from all other point sources), and at the same time underestimate the point source amplitude. Scanning of complicated models in this way also takes forever, so there is no way this technique can be used to do detailed background or spectral fits. We therefore apply it only for determining the existence and approximate location of point sources. We then turn to differential evolution for carrying out detailed fits and profile likelihoods of the spectral parameters of sources identified with Bayesian object detection, and for determining background and DM parameters.

### 5.3.3 Point source parameter estimation

To fit the parameters of point sources after identifying them with MultiNest, we use a genetic-inspired optimisation algorithm, Differential Evolution, as implemented in the code DIVER. In a nutshell, it makes a population of individual parameter points, treats them as vectors within the parameter space, and evolves the population towards better fits by carrying out various vector addition, subtraction and replacement operations on the different vector components of different individuals. This evolutionary process includes a mutation element, and depends on the whole population, allowing the fittest individuals to evolve towards the parameter combination returning the highest likelihood. The idea is to find the point sources' positions with MultiNest, and then fit all the parameters of those sources with Diver, hoping for a better accuracy. This seems to work pretty well from the tests that we have done so far (details below).

### 5.3.4 Unified fit strategy

Our overall iterative fitting method is thus as follows:

1. Background (simple 3D parameterisation:  $T_S$ ,  $X_{CO,global}$ ,  $globalnorm(p)$ ) and point source fit (3 parameters ( $l, b, N_0$ ) high energy bins only). Posterior scan (MultiNest), 6D.
2. Background (simple 3D parameterisation) fit for null evidence. Posterior scan (MultiNest), 3D.
3. Background (full 11D parameterisation) and point source fit (5 parameters, high and low E bins, with positions fixed to best-fit values from step 1), with Known Point Source Index discrete parameter, iteratively setting parameters of point sources \*not\* corresponding to the value of the index parameter to their current best-fit values as the scan progresses and those best-fit values improve. Gradually improves the fits of the known point sources. Likelihood-only scan (Diver), 17D.
4. Repeat Steps 1–3, with found PS and 8 non-simple BG values fixed to their best fit values from Step 3 when repeating Step 1. Repeat until all point sources seem to have been found, i.e. no more pass the null evidence cut.
5. Repeat steps 1 and 2 also including low energy bins, to make sure we didn't miss any PS that don't show up in the high E bins. If we did miss any, run them through steps 3 and 4 to get their parameters.
6. Repeat step 3 one last time, including all PS found to this point, and also allowing their positions to vary. The point sources should start the fit with their current best-fit values.
7. Calculate the local evidence for each PS (i.e. find the difference in the evidence found when including all PS, and when excluding a certain PS

from the model). Discard the ones that don't pass the evidence threshold (**PS: this threshold still to be defined**).

8. Fix the point source parameters to the best fit values. Background (full 11D parameterisation) and DM fit (full 15D parameterisation). Likelihood-only scan (Diver), 26D.

### 5.3.5 Results of point-source tests

To test the ability of our unified fit strategy (5.3.4) to accurately recover point sources, we implemented a full simulation facility in DMBAYES a la *gtobssim*, as well as routines to access the 2-year LAT point-source catalogue as a source of mock point sources.

#### Steps 1-2

**Test 1** (Charlotte): Results for a point source identification scan in a fixed background are shown in Fig. 26. Parameters scanned over are the two position parameters and the amplitude, i.e. the spectrum of the PS is fixed. The scan includes all 46 PS extracted from the catalogue (corresponding to roughly  $4\sigma$  sources). Point sources marked in blue are found by the scan and their parameters are correctly identified (i.e. the amplitude is off by at most 0.1 log units). Pink sources are found by the scan, but their best-fit amplitude is different from their true amplitude. For all of these mismatched PS the difference between true and best-fit amplitude is  $\Delta \log(N_0) \leq 1.0$ . Point sources shown in red were not found by the scan. Note that all of the missed PS correspond to a relatively low amplitude  $\log(N_0) \leq -12.0$ . Results are quite encouraging, but unsurprisingly the Galactic Centre region is very challenging. Iterative application of this technique after fitting the parameters of the found sources should clear up most of the poor fits and missing sources.

**Test 2** (Anotoine):

- MultiNest 6D, first run
- ini file: 46PS\_6DMNRunI.ini<sup>1</sup>
- nCdims = 2, nlive = 4000, tol = 0.02, eff = 0.3
- Null evidence ini file: MNNullRunI.ini

31 modes were found, of which 4 were discarded by the Null evidence (i.e. they have a local evidence strictly lower than the global evidence found in the Null run). Figure 27 shows  $\chi^2 = -2\text{Log}(\text{Likelihood})$  as a scatterplot in  $(l, b)$  after this run, featuring the true point sources. At this stage, one can see that 9 point sources are missed by the scan, and some that lie close one to each other are not separated out.

---

<sup>1</sup>To remake those runs on the HPC with walltime = 72hrs, one will need to restart and continue, i.e. to change the `restart_and_continue` from F to T in this ini file after 72 hrs.

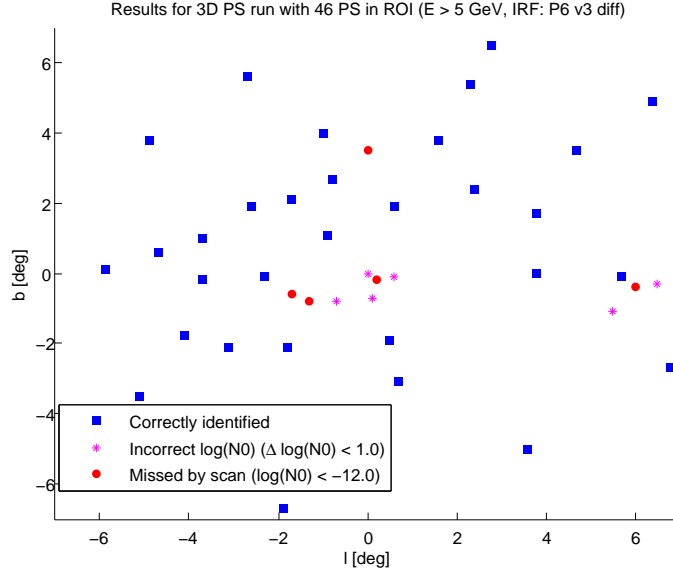


Figure 26: Results for the identification of PS in a fixed background, scanning only over the two position parameters and the amplitude, and discarding information from the first 9 energy bins.

### Step 3

**Test 1** (Grace): details not shown – good fits obtained with up to 10 point sources, bugs encountered thereafter. Bugs fixed. Plotting scripts and ini files passed on to Antoine.

**Test 2** (Antoine): We tested the efficiency of Step 3 with a fake data set generated from the 46 PS from the catalogue, in a set background (3rd grid point, all templates not rescaled, i.e.  $x_S = -49.6$ ,  $X_{CO,global} = 1$ ,  $norm_e = norm_p = 1$ ,  $index_e = index_p = 0$ ,  $\alpha = 2$ ,  $\beta = 5$ ). The ini files referred to here can be found in `antoine_for_the_record/46PS/ini_files/` on the svn main directory.

These tests were Diver 11D runs (3D for the BG, 7D per PS and 1D: PS index).

- ini file: `46PS_11DDiverRunI.ini`
- follow up file: `27modes_above_nullev.txt`

I set `gen_tol_smooth_len = 300` (=number of generations) in this run to pre-



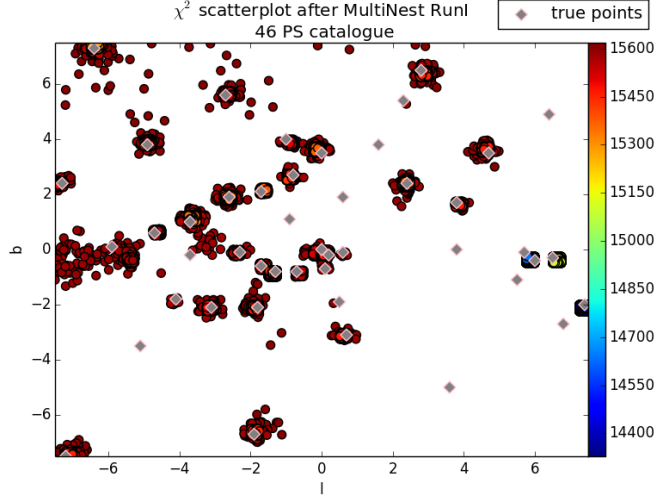


Figure 27:  $\chi^2$  scatterplot after MultiNest 1st run for the 46PS with BG

vent Diver from stopping when the convergence criterion is wrongfully fulfilled<sup>2</sup>. One point source never fell in the allowed box in  $l, b$  around the position determined from the MultiNest run in Step 1<sup>3</sup>, and the others converged properly (see figures 28 and 29). More plots from this run, including the scatter plots in projections of the parameter space for each point source, are in `for_the_record/figures/DiverI/` (and in `DiverI_extended`, are those plots for a greater value of `maxgen`. They are given for comparison – the best fits used for the second run of MultiNest are the ones from `DiverI`, and there is no substantial improvement between generation 300 and 400). The results are not fully satisfying: a few point sources are “well fitted”, but for most of them there is a sizeable discrepancy between the true and best fit values of  $\alpha$ ,  $\beta$ ,  $N_0$  and  $E_0$ : see table 3 (probably the plots from the `DiverI` directory are a bit clearer). Still, it is only the first iteration of Step 3, and only 27 point sources are fitted to account for a map with 46 at this point, so it would have been surprising to find a perfect fit for those points straight away.

#### Step 4 (repeat of 1+2)

- MultiNest 6D, RunII

<sup>2</sup>The convergence criterion is: no improvement in the mean likelihood amongst all subpopulations during `gen_tol_smooth_len`, but if a subpopulation (point source) does not fall into the allowed  $l, b$  range, its `logLike`  $\sim \infty$  which numbs the effect of the other subpopulation's improvement. Setting `gen_tol_smooth_len=maxgen` keeps this criterion from being reached during the whole run.

<sup>3</sup>This should no longer happen now, as the prior for Diver is no longer ‘LogZero’ everywhere outside the allowed box, but something like `logZero*(1+distance from allowed box)`

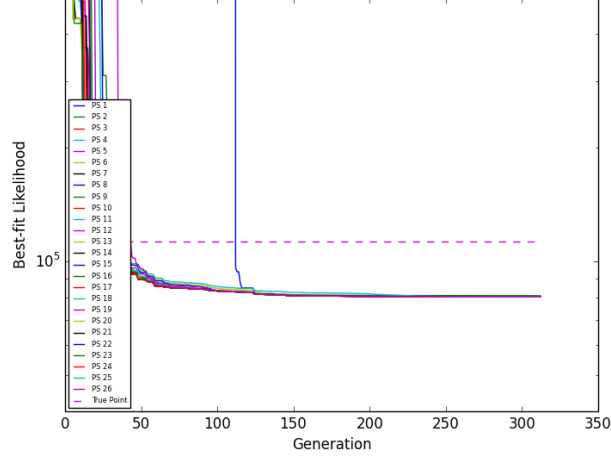


Figure 28: Best fit likelihood for Diver first run (Step 3) with 46 PS. The dashed line is meaningless here (does not actually corresponds to the true point value)

- ini file: 46PS\_6DMNRunII.ini
- Null evidence: MNNullRunII.ini
- nCdims = 2, nlive = 3000, tol = 0.01, eff = 0.3

The 26 point sources fitted by DIVER in the previous step are now added to the model<sup>4</sup>, to find the left point sources on top. So far (the run is not finished yet), MultiNest has found 14 modes, but unfortunately it does not seem to be any of the ones missed in the first run, but either points that lie close to one previously found, or just “another finding of one same point source” (if, for example, its amplitude has been underestimated in steps 1 to 3) : see figure 30. We can hope to find the rest of the point sources in further iterations of steps 1-3 (with more live points/lower tolerance?), or perhaps when adding the low energy bins.

<sup>4</sup>This is currently hardcoded in calclike.f90 - search '!AR' comments to find where exactly.  
**PS: I will implement new code that allows this to be automated from step to step.**

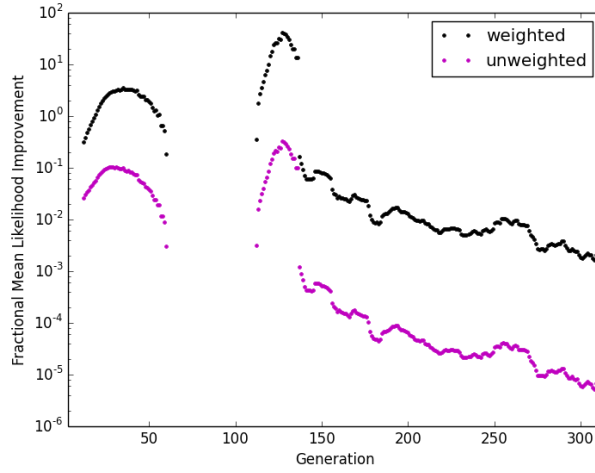


Figure 29: Convergence Criteria for Diver first run (Step 3) with 46 PS. The weird features before generation 130 are due to points not yet in the allowed  $l, b$  range (the missing points are 0., since there is no likelihood change during a period at which all points but one have fallen into the allowed range)

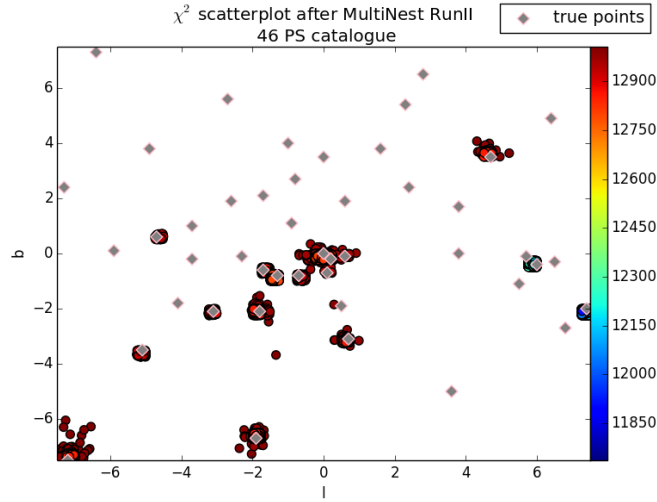


Figure 30:  $\chi^2$  scatterplot after MultiNest 2nd run for the 46PS with BG

| PS | $l$         | $b$         | $N_0$         | $E_0$       | $\alpha$    | $\beta$     | $1.e5/E_C$    |
|----|-------------|-------------|---------------|-------------|-------------|-------------|---------------|
| 1  | -4.9 (-4.9) | 3.8 (3.8)   | -12.9 (-12.3) | 2645 (1894) | 1.11 (2.24) | 0.38 (0.00) | 0.05 (0.00)   |
| 2  | 5.1 (4.7)   | 4.4 (3.5)   | -10.4 (-11.4) | 613 (878)   | 0.67 (2.43) | 0.71 (0.00) | 268.54 (0.00) |
| 3  | -2.5 (-2.7) | 5.5 (5.6)   | -12.6 (-11.4) | 718 (730)   | 0.09 (2.45) | 0.48 (0.00) | 0.46 (0.00)   |
| 4  | 2.9 (2.8)   | 6.4 (6.5)   | -11.8 (-12.0) | 966 (1353)  | 1.86 (2.30) | 0.15 (0.00) | 0.01 (0.00)   |
| 5  | -7.3 (-7.3) | 2.3 (2.4)   | -12.7 (-10.8) | 4604 (996)  | 2.33 (2.51) | 0.12 (0.25) | 22.08 (0.00)  |
| 6  | -1.2 (-1.7) | 2.1 (2.1)   | -12.7 (-12.3) | 572 (2159)  | 1.18 (2.26) | 0.88 (0.00) | 8.99 (0.00)   |
| 7  | 7.3 (6.5)   | 1.7 (-0.3)  | -13.2 (-10.4) | 559 (1411)  | 2.42 (2.39) | 0.93 (0.35) | 100.72 (0.00) |
| 8  | 1.3 (-0.0)  | 3.8 (3.5)   | -11.6 (-12.0) | 1129 (1633) | 2.10 (2.30) | 0.69 (0.00) | 199.48 (0.00) |
| 9  | 7.1 (6.5)   | -0.3 (-0.3) | -12.6 (-10.4) | 1815 (1411) | 2.99 (2.39) | 0.00 (0.35) | 135.80 (0.00) |
| 10 | 6.5 (5.7)   | -0.3 (-0.1) | -11.1 (-11.5) | 3058 (1902) | 2.94 (2.55) | 0.40 (0.44) | 9.61 (0.00)   |
| 11 | 4.0 (3.8)   | 1.6 (1.7)   | -11.8 (-11.2) | 2803 (1643) | 1.97 (2.30) | 0.47 (0.37) | 11.55 (0.00)  |
| 12 | -0.6 (-0.0) | -0.5 (-0.0) | -12.4 (-10.4) | 4874 (1618) | 1.41 (2.34) | 0.00 (0.25) | 69.57 (0.00)  |
| 13 | -0.2 (-0.0) | -0.5 (-0.0) | -12.1 (-10.4) | 4691 (1618) | 1.01 (2.34) | 0.00 (0.25) | 98.72 (0.00)  |
| 14 | -0.7 (-0.9) | 1.1 (1.1)   | -10.6 (-10.5) | 908 (813)   | 0.99 (2.70) | 0.16 (0.68) | 220.09 (0.00) |
| 15 | -2.0 (-0.9) | 0.2 (1.1)   | -12.0 (-10.5) | 1734 (813)  | 0.50 (2.70) | 0.27 (0.68) | 384.45 (0.00) |
| 16 | -3.7 (-3.7) | 1.0 (1.0)   | -12.0 (-10.6) | 4837 (1302) | 2.99 (1.11) | 0.60 (0.00) | 13.09 (49.50) |
| 17 | -2.3 (-2.6) | 1.9 (1.9)   | -12.9 (-12.0) | 687 (1913)  | 0.34 (2.26) | 0.14 (0.00) | 343.61 (0.00) |
| 18 | 2.3 (2.4)   | 2.5 (2.4)   | -12.6 (-12.1) | 2629 (1832) | 1.81 (2.20) | 0.06 (0.00) | 0.93 (0.00)   |
| 19 | -1.0 (-0.8) | 2.6 (2.7)   | -11.9 (-11.9) | 1365 (1545) | 2.33 (2.39) | 0.00 (0.00) | 0.04 (0.00)   |
| 20 | -1.6 (-1.7) | 2.1 (2.1)   | -12.1 (-12.3) | 1454 (2159) | 1.81 (2.26) | 0.06 (0.00) | 0.91 (0.00)   |
| 21 | -2.6 (-2.6) | 1.8 (1.9)   | -12.3 (-12.0) | 1860 (1913) | 1.54 (2.26) | 0.20 (0.00) | 0.03 (0.00)   |
| 22 | -3.5 (-2.6) | 1.4 (1.9)   | -13.0 (-12.0) | 824 (1913)  | 0.73 (2.26) | 0.63 (0.00) | 420.30 (0.00) |
| 23 | -0.2 (-1.0) | 3.6 (4.0)   | -11.4 (-11.5) | 658 (907)   | 1.49 (2.52) | 0.18 (0.00) | 0.01 (0.00)   |
| 24 | -0.8 (-0.0) | 4.0 (3.5)   | -12.3 (-12.0) | 827 (1633)  | 0.08 (2.30) | 0.60 (0.00) | 0.04 (0.00)   |
| 25 | -6.5 (-6.4) | 7.4 (7.3)   | -12.5 (-11.5) | 1196 (1043) | 2.10 (2.24) | 0.80 (0.00) | 6.45 (0.00)   |
| 26 | -6.4 (-6.4) | 7.3 (7.3)   | -13.2 (-11.5) | 6097 (1043) | 1.89 (2.24) | 0.09 (0.00) | 1.77 (0.00)   |

Table 3: best fit (true value) for each point source parameter after Diver first run.

### Step 5 (test 1 to 4)

(Andrea) The MultiNest run found 28 point sources, only 17 of which had Local Evidence strictly higher than the Global Evidence in the null hypothesis (3D MultiNest scan). Those point sources are shown in the Fig. 31. The adopted parameters are the following:

- nCdims=2 (corresponding to  $l, b$ )
- live=3000
- eff=0.3
- tol=0.01

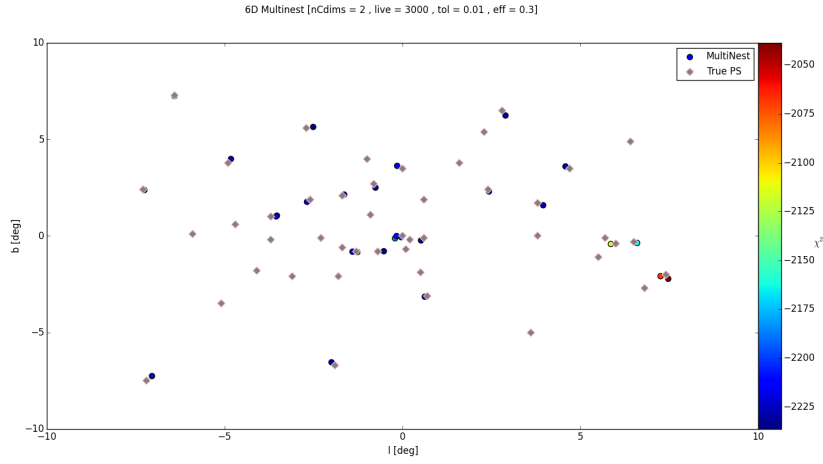


Figure 31:  $\chi^2$  scatterplot of 17PS found after MultiNest 1st run against the 46 true PS

The 17 MultiNest-found point sources have then been input into Diver, which returned their best-fit parameters, separating the 1/3 brightest of these in a different output file to be then used as model input in the next iteration of MultiNest. The result of this run, for all 17 point sources, is shown in Fig. 32. This figure clearly displays the presence of an issue with Diver as some MultiNest (reasonably well) fit point sources' position are best-fit far away from the corresponding true point source position. The probable underlying explanation is an attempt by Diver to simultaneously fit two nearby point sources with a single one accounting for the emission of both. This problem can be due to the broadening of the IRF at low energies, leading to the overlap of two neighbouring point sources at the low energy bins which, differently from MultiNest, are examined by Diver.

This issue has urged the following modification in the UFS: Decrease the di-

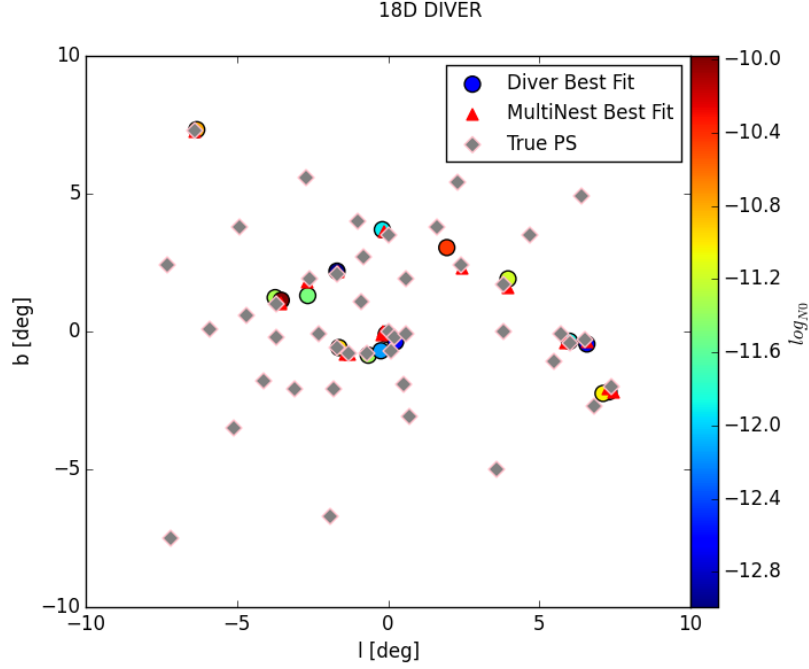


Figure 32:  $\chi^2$  scatterplot after MultiNest 1st run for the 46PS with simple (3D) BG

dimensionality of the parameter space scanned for each PS by Diver from 19D to 17D, where the position of each PS is to be kept fixed at the MultiNest-found values. This will avoid the point sources from being shifted away from the true PS position while still providing an improved spectral fit. At the final iteration of MultiNest - i.e. when no more found point source passes the Global Null Evidence - Diver is run one final time letting the full 19D parameter space of all point sources to be examined.

## 6 To do

### 6.1 Things missing from these notes

- Comment about treatment of extended sources in our ROI (such sources do show up in 2FGL catalogue)
- Add some information on DM profile parameters (3 generalised NFW, 1 local DM density)
- Add brief results of the BG reconstructions Charlotte did
- Add brief results of the PS reconstructions Grace did

## 6.2 Remaining analysis design issues

- What is a reasonable value to use in Step 6?
- Should we use front-converting events or both front- and back-converting events? (Use one at low and one at high energies? This would slow down the runs, since we have to store twice as many files in memory.)
- Pass 8?

## 6.3 Outstanding code implementations

- Re-jig code to seamlessly operate any of the steps in Sec 5.3.4, without recoding each time (Pat)
- Discard faintest 2/3 of point sources found in each iteration of Step 1 before moving on to Step 3 (Pat)
- Add Fermi bubble template (+obtain from Meng Su / Christoph W)
- Set the EGBG normalisation in the diffuse model database index file
- Decide on final resolution of undefined pixel error in BG maps Gulli sent
- Get new simulated data files with the correct resolution and starting at 300 MeV (instead of 100 MeV). **PS: Not sure if this actually still needs doing?**
- Analyse 2 or more years of real Fermi data

## 6.4 Tests still to be completed

Definitely to be done:

- Test Steps 1-4 fully run through to convergence (current tests only include 3D BG in Step 3, lack a bubble template, do not discard the fainter 2/3 of sources after Step 1, and are not yet converged wrt Step 4.)
- Test Step 5
- Test run of a BG + DM reconstruction (Step 7)
- Test run of a BG + DM + PS reconstruction (Step 7)

Previously planned **PS: and not sure if we need to actually do or not:**

- Test the reconstruction procedure on the point sources map from Simona **CS: Roberto, are we still planning to do this? Have you heard from Simona about this?**
- Test reconstructions using DM profile nuisance params
- Test the prior on the annihilation cross-section in a DM only scan using the mapcubes Tesla sent